Nuclear Instruments and Methods in Physics Research A 771 (2015) 55–65

Contents lists available at ScienceDirect

Nuclear Instruments and Methods in Physics Research A

journal homepage: www.elsevier.com/locate/nima

Inverted-conical light guide for crosstalk reduction in tightly-packed scintillator matrix and MAPMT assembly

Y.-Y. Chang [a,b,*], C.R. Chen [c], P. Chen [a,b], J.-J. Huang [a,b], M.A. Huang [b,d], T.-C. Liu [b], J.W. Nam [a,b], M.-Z. Wang [a,b], V. Bogomolov [e,f], S. Brandt [g], C. Budtz-Jørgensen [g], A.J. Castro-Tirado [h], H.S. Choi [i], P.H. Connell [j], C. Eyles [j], S. Jeong [h], J.E. Kim [k], M.B. Kim [k], S.-W. Kim [l], J. Lee [k], H. Lim [k], K.W. Min [m], M.I. Panasyuk [e,f], I.H. Park [k], V. Petrov [e], V. Reglero [j], J. Řípa [n], J.M. Rodrigo [j], S. Svertilov [e,f], I. Yashin [e]

[a] Department of Physics, National Taiwan University, 1 Roosevelt Rd., Taipei 10617, Taiwan, ROC
[b] Leung Center for Cosmology and Particle Astrophysics, National Taiwan University, 1 Roosevelt Rd., Taipei 10617, Taiwan, ROC
[c] National Space Organization (NSPO), 8F., No. 9, Prosperity 1 s Rd., Hsinchu Science Park, Hsinchu 30078, Taiwan, ROC
[d] Department of Energy Engineering, National United University, 1, Lienda, Miaoli 36003, Taiwan, ROC
[e] Skobeltsyn Institute of Nuclear Physics of Lomonosov Moscow State University, Leninskie Gory 119234, Russia
[f] Physics Department of Lomonosov Moscow State University, Leninskie Gory 119234, Russia
[g] National Space Institute, Astrophysics, Technical University of Denmark, DK-2800 Kongens, Lyngby, Denmark
[h] Instituto de Astrofisica de Andalucia (IAA-CSIC), Glorieta de la AstronomÃ a, s/n, E-18008, Granada, Spain
[i] Korea Institute of Industrial Technology, 89 Yangdaegiro-gil, Seobuk-gu, Cheonan-si, Chungcheongnam-do, 331-822, Korea
[j] Image processing Laboratory (IPL), University of Valencia, C/ Catedratico J. Beltran, 2 E-46980, Paterna, Spain
[k] Department of Physics, Sungkyunkwan University, 2066 Seobu-ro, Suwon 440-746, Korea
[l] Center for Galaxy Evolution Research & Department of Astronomy, Yonsei University, 134 Shinchon-dong, Seoul 120-749, Korea
[m] Department of Physics, Korea Advanced Institute of Science and Technology, 291 Daehak-ro, Daejeon 305-701, Korea
[n] Institute of Basic Science, Sungkyunkwan University, 2066 Seobu-ro, Suwon 440-746, Korea

The UFFO Collaboration

ARTICLE INFO

Article history:
Received 31 July 2014
Received in revised form
7 October 2014
Accepted 20 October 2014
Available online 29 October 2014

Keywords:
Light guide
MAPMT
YSO
Crosstalk
GEANT4 simulation

ABSTRACT

In this paper we present the Inverted-Conical light guide designed for optical crosstalk reduction in the scintillator-MAPMT assemblies. The research was motivated by the 30% crosstalk observed in *UFFO* X-ray telescope, *UBAT*, during the preliminary calibration with MAPMTs of 64 2.88×2.88 mm^2 pixels and identically gridded YSO crystal matrices. We began the study with the energy and crosstalk calibrations of the detector, then we constructed a GEANT4 simulation with the customized metallic film model as the MAPMT photocathode. The simulation reproduced more than 70% of the crosstalk and explained it as a consequence of the total reflection produced by the photocathode. The result indicated that the crosstalk mechanism could be a common case in most of the contact-assembled scintillation detectors. The concept of the Inverted-Conical light guide was to suppress the total reflection by contracting the incident angle of the scintillation. We optimized the design in the simulation and fabricated a test sample. The test sample reduced 52% crosstalk with a loss of 6% signal yield. The idea of the Inverted-Conical light guide can be adapted by scintillation detectors multi-pixel, imaging-purpose scintillation detectors such as the ultra-fast GRB observatory *UFFO-UBAT*, whose performances are sensitive to responding time, image resolution, and geometrical modifications.

1. Introduction

1.1. UFFO project

Ultra-Fast Flash Observatory (*UFFO*) is a space-borne observatory aiming to detect the early emission of the Gamma-ray bursts (GRBs) [2]. It will be installed on-board Moscow State University satellite *Lomonosov* schedule for launch in 2015. With its ultra-fast slewing

* Corresponding author at: Department of Physics, National Taiwan University, 1 Roosevelt Rd., Taipei 10617, Taiwan, ROC.
E-mail addresses: gixd@hep1.phys.ntu.edu.tw (Y.-Y. Chang), mzwang@hep1.phys.ntu.edu.tw (M.-Z. Wang).

http://dx.doi.org/10.1016/j.nima.2014.10.037
0168-9002/

capability, *UFFO* can start its follow-up UV–optical observation 1–2 s after the X-ray prompt triggers. Even in other fast GRB observatories, e.g. *Swift*, GRB UV–optical (afterglow) data is mostly taken 50–100 s after the prompt triggers. *UFFO* is hopefully the first space observatory delivering the sub-minute afterglow data [1,2].

Many exciting physics topics are waiting to be discussed for the first time with the sub-minute afterglow. Some are seen with salient hints and are urgently needing the confirmation with even earlier light curves, e.g. Panaitescu et al. [3] suggests that Supernovae (SNe) may serve as the new "recalibratable standard candles" based on the early afterglow obtained by the *Swift*; Page et al. [4] points out, according to a few peculiarly bright events like GRB 080810 observed with the prompt-emission-like structure in the rather early afterglow light curves, the internal–external shock unification model may be tested with the data of the earlier mixing phase of the prompt emission and the afterglow, which in principle exists in all early light curves. Others are simply hypothetical but lack supporting data, e.g. the (non-)existence of the short-hard burst (SHB) afterglows, which quickly decay into dimness before any former experiment starts its optical observation, the progenitor modeling of the SHBs, the (non-)existence, origination or even classification of the dark bursts. And most of all, completion to the long anticipated "blind time" data lays between the end of the prompt emission and the start of the former optical-UV observations [2,5–7].

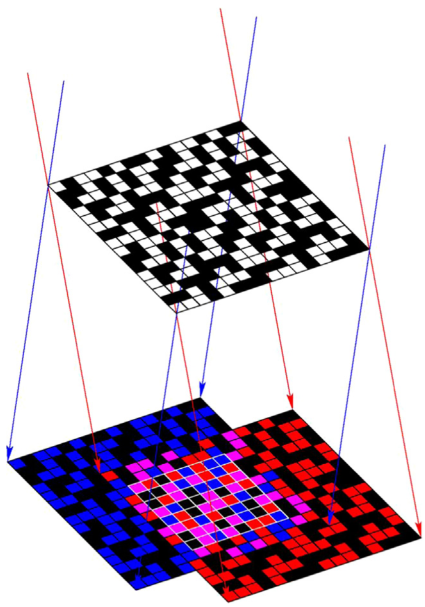

Fig. 1. An illustration to the principle of the coded mask aperture camera scheme. The black-and-white matrix on top is the γ-ray-impenetrable coded mask, the projection plan at the bottom is the focal surface (FS). The blue and the red projections represent the full mask images of two different events (blue and red areas may be gray if you are reading a hard copy paper). The white-lined square area at the center represents the sensitive area of FS where the images are actually visualized. By comparing the pre-loaded coded mask pattern to the partially visualized images, the event directions may be discerned. Note that as the incident angle rises, the legible fraction of the mask's projection decreases [11]. (For interpretation of the references to color in this figure caption, the reader is referred to the web version of this article.)

1.2. Design of UFFO-p and UBAT

Ultra-Fast Flash Observatory, as it is named, is built to be the fastest ever UV-optical observatory that triggers on the transient X-ray sources, and *UFFO pathfinder* (*UFFO-p*) is the first attempt in *UFFO*. It is composed of two major telescopes: *UFFO Burst Alert and Trigger Telescope* (*UBAT*) and *Slewing Mirror Telescope* (*SMT*). They coordinate the full operation of *UFFO-p*. Fig. 2 is the schematics of *UFFO-p*.

UBAT is equipped with a wide field of view (FOV) and serves as the primary trigger telescope responsible for 10–150 keV prompt X-ray observation. *UBAT* operates under the coded mask aperture camera scheme similar to *Swift-BAT* (Fig. 1) [9,10].

Once a GRB occurs in *UBAT* FOV, the coded mask pattern is projected on to the focal surface (FS) of *UBAT*. Through recognizing the location of the mask pattern, i.e. the location of the X-ray image, *UBAT* determines the event direction immediately and forwards it to *SMT* for follow-up UV/optical aiming. *SMT*'s ultra-fast response is realized through utilization of the Slewing Mirror Telescope (SMT) [8]. Unlike all the predecessors which rotate the entire optical instruments to aim the GRBs, *UFFO-p* SMT slews its lightweight mirror to redirect the light path into the telescope in

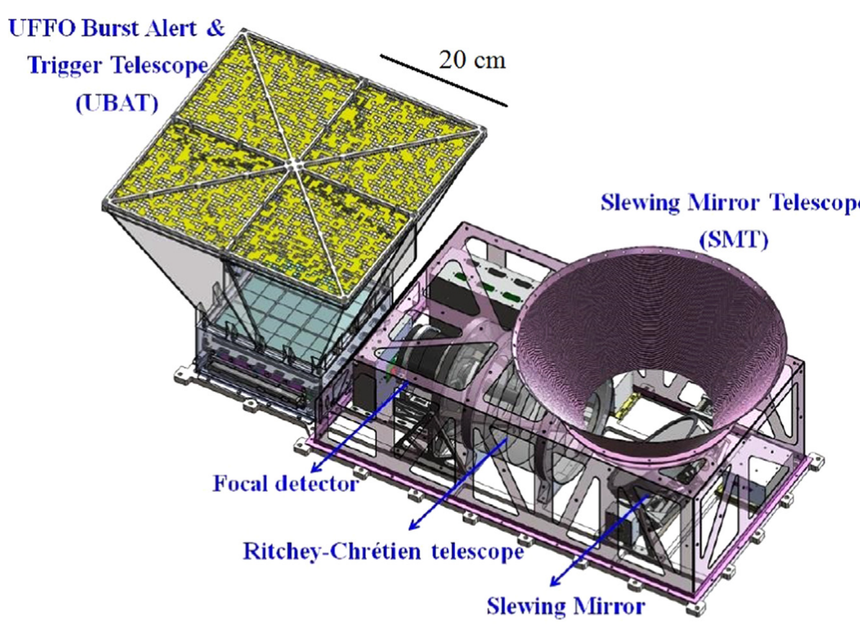

Fig. 2. The schematics of *UFFO-p*. The square tapered coded mask camera telescope on the left is *UBAT*. The encased *SMT* is on the right, with the slewing mirror beneath the round tapered window and the Ritchey–Chretien telescope in the case.

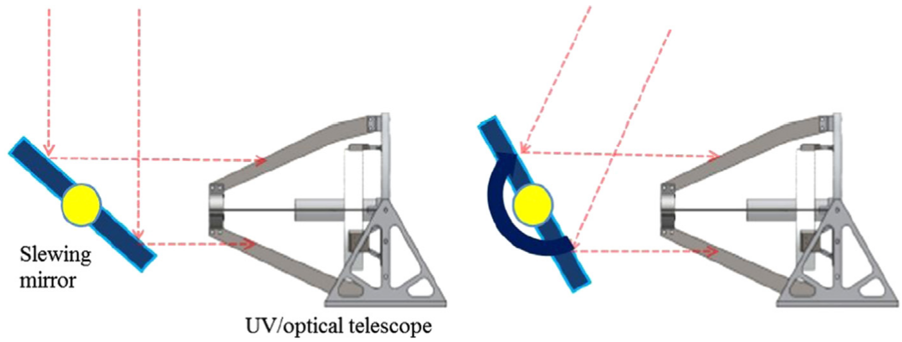

Fig. 3. An illustration to the concept of SMT. The UV/optical signals are redirected into the stationary telescope by the slewing mirror [8].

an instant. The innovation improves the 100 s limitation of *Swift* to 1 s [2,8,9]. Fig. 3 illustrates the concept of SMT.

In order to increase the success rate of the narrow-FOV aiming of UV–optical observation in *SMT*, it is crucial *UBAT* determines the precise GRB locations from the X-ray coded mask image fast and accurate. To that end, UBAT must obtain a clearly resolved coded mask image, i.e. clearly discriminates the γ-hit/non-hit signals on FS.

This paper is organized as follows: we first present the calibration of *UBAT* focal surface (FS) in Section 2, where the signal yield and the situation of the high signal crosstalk among pixels is reported. This work was motivated by the $\sim 30\%$ crosstalk signal height found in the pixels surrounding the X-ray-photon-illuminated pixel. The purpose of this study was to search for possible solutions to reduce the crosstalk-to-signal ratio for better mask pattern recognition with possible enhancement to the absolute signal yield. To resolve the causes of the crosstalk, we built the simulation of *UBAT* FS, which is discussed in Section 3. Once we understood the mechanism of the crosstalk, we were able to propose the Inverted-Conical light guide. In Section 4, we introduce the concept and optimization of Inverted-Conical light guide. It was specialized to cope with the reflection-caused crosstalk, which could be a common problem in touching-assembled scintillation detectors. We then fabricated the test sample to put the idea to a further validation. The result is reported in Section 5. Inverted-Conical light guide was proven to reduce the crosstalk and potentially enhance the signal yield. The conclusion is provided in Section 6.

1.3. *UBAT focal surface components*

In this paper we utilized the FS detection units[1] of *UBAT* as our X-ray scintillation detector. *UBAT* FS is composed of 36 assemblies of Yttrium Oxyothosilicate (YSO) scintillator arrays and the multi-anode photomultiplier tubes (MAPMTs) (Fig. 4). The detection units connect to the electronics underneath in a 6×6 matrix. The total sensitive area is $13.82 \times 13.82\ \text{cm}^2$, i.e. $191.1\ \text{cm}^2$.

The scintillator array is an 8×8 integration of 64 $2.68 \times 2.68 \times 3\ \text{mm}^3$ Cesium-doped YSO (Y_2SiO_5:0.2% Ce) crystal cubes. To enhance the collectivity of the scintillation photons and improve the imaging quality, 200 μm dielectric mirror reflector films are attached between the crystal cubes. A 70 μm reflector covers the entire non-MAPMT-coupling surface. The scintillator is designed to match the pixel geometry of the MAPMT, and each YSO crystal cube aligns its corresponding MAPMT pixel at the center while coupled. Table 1 lists the characteristics of the YSO crystal.[2]

UBAT utilizes Hamamatsu *R11265-03-M64* MAPMT which is specialized for the imaging purposes in space scientific missions. The *UFFO* collaboration has demonstrated that *UFFO-p*, including the delicate MAPMTs and other optical components, can survive the launch and the space environment with a series of space-mimic tests [2]. Table 2 lists the parameters of *UBAT* MAPMT. It has two special features: First, *UBAT* MAPMT does not implement any insensitive gaps between the photocathode pixels. This modification from its predecessor not only enlarges the packing factor of the sensitive region by about 30%, but also enhances the evenness of detection efficiency and imaging quality on the surface. Second, *UBAT* MAPMT equips the newly developed photocathode compound. The Quantum Efficiency (QE) of the old material was $\sim 25\%$ at the YSO scintillation peak, and it is $\sim 35\%$ of the new compound.

1.4. *Review on light guide design*

Fig. 5 is an example of a traditional design of light guides (LGs). It intuitively matches the sizes of the scintillator and the photon detector at two ends and serves as a funnel that collects photons through internal reflection. By recovering the photons that would have been lost, the size-coupling design may enhance the signal significantly. But the design generally suffers from a signal drawback as the length grows [24]. However, it is usually impractical to implement too short a size-coupling LG, e.g. shallower than the crystal size, when the optical-caused crosstalk is to be concerned. A shorter LG implies a sharper-sloped funnel shape, which redirects the scintillation light with larger incident angles and a wider area of illumination. An example of the possible solution is also presented in Fig. 5. By absorbing the redirected light at large angle, the signal uniformity can be regained to some level. But the signal yield is again compromised [25].

Another example of image modulator is the *micro-lens array* (MLA) (Fig. 6) [26–28]. It is basically an array of identical lenses. Through advanced engineering, the lenses can be made 10–100 μm in sizes with customized concave or convex curves. There are several advantages of MLA. First, it may possess the identical optical functionality of the one-piece lens, e.g. focusing or diverting the light, but be much thinner in thickness. Second, if the photon detector used is multi-pixel, the arrangement of lens array may be customized to be one-pixel-to-one(several)-lens. The major problem of MLA is it is obviously delicate and cost-unfriendly. Considering the drawback, MLA seems impractical for space missions such as *UFFO*.

2. Focal surface calibration

2.1. *Method*

All the experiments performed in this paper were conducted in the laboratory environment under normal atmospheric pressure,

[1] We will frequently address one scintillator matrix-MAPMT assembly as a detection unit.

[2] Items without the references mentioned are provided by the manufacture.

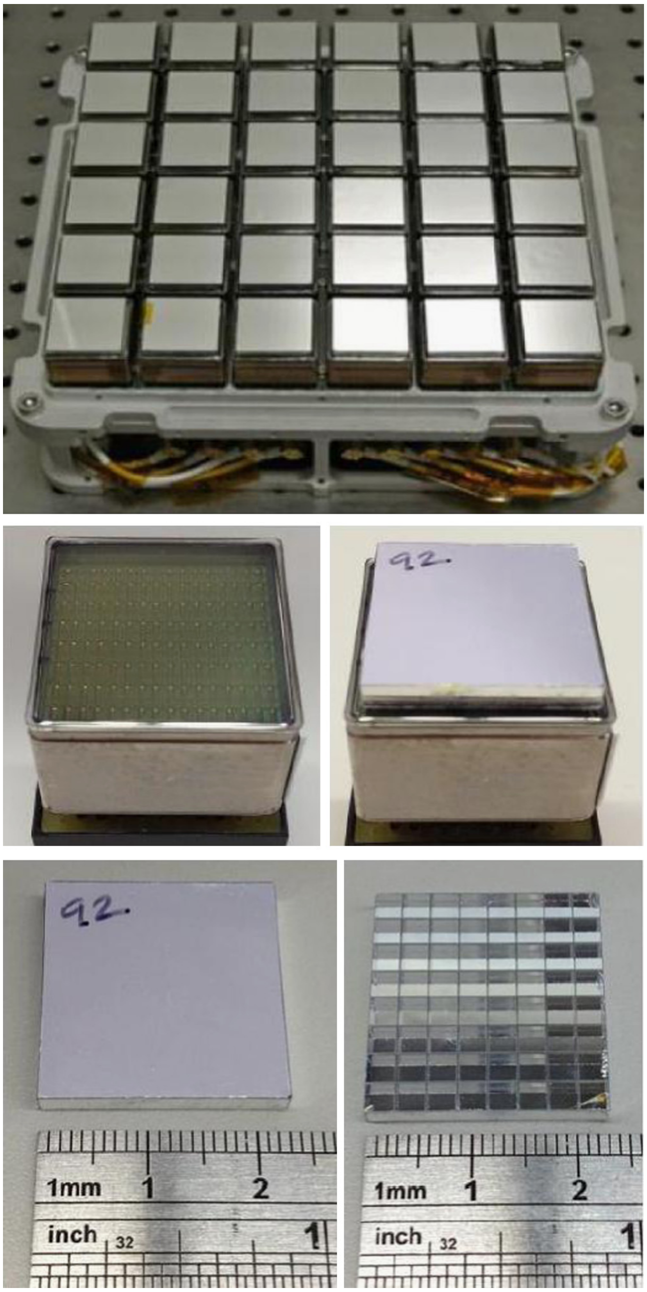

Fig. 4. The photos of the complete construction of *UBAT* FS and the electronic box (top), the MAPMT and the detection unit (middle), and the front and the back side of the YSO scintillator array (bottom). The dimensions may be inferred from the reference shown in the photos.

Table 1
The specification of *UBAT* YSO crystal.

Density (g/mm^3)	4.45
Peak scintillation (nm)	400
Index of refraction (at 400 nm)	1.8
Scintillation time constants (ns)	35 [12]
Photon yield (γ/keV)	9.2 [13]

23 °C. Every contact interface between the optical components, e.g. MAPMT, scintillator and light guide, was coupled by Dow – Corning® Q2-3067 optical couplant. A $25\times25\times180\ \mathrm{cm}^3$ light-tight aluminum cabinet was prepared for the experiments. The interior and the fixtures inside were covered by the black flannel blanket to eliminate reflections. The calibration sources, e.g. LED and radioactive sources, were situated 80–160 cm away from the detection unit. Regarding the calibration sources point-like, the divergent angles of the illuminations were $\pm0.4^\circ$–$\pm0.7^\circ$ on the frontal surface of the detection unit.

Table 2
The specification of *UBAT* MAPMT.

Window geometry (mm^3)	$26.2\times26.2\times0.8$
Window material	UV-enhanced glass
Pixel arrangement	8×8
Pixel size (mm^2)	2.88×2.88
Pixel material	Super-Bialkali
Pixel gapping	None
Operation high voltage (V)	900

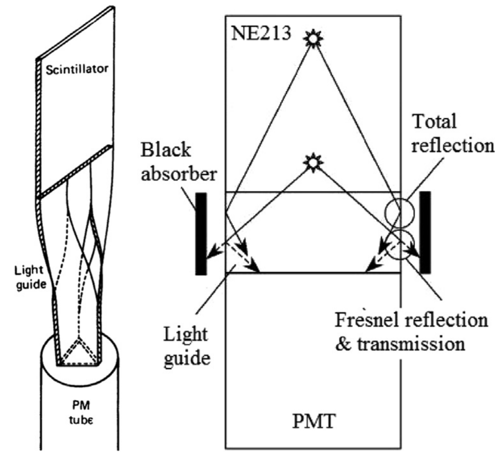

Fig. 5. Left: the traditional size-coupling LG. Right: a large-angle-incident-absorbing uniformity enhancing LG [24,25].

We used the data acquisition (DAQ) system developed by *NuTel* experiment as the MAPMT DAQ [14–17]. The DAQ system was capable of simultaneously taking data from 512 MAPMT channels in the range of 0–1000 photocathode-emitted photoelectrons (PEs) up to 1500 Hz. We calibrated the signal gain of each channel separately and designated 0.33 PE to be the trigger threshold.

We applied a collimator on the detection unit, so the calibrating X-ray photons could only illuminate one of the central pixels (Figs. 7 and 8). The collimator was a Lead plate 3 mm in thickness with a ϕ1.0 mm pin hole at the center of Ch. 27. The triggers from all the non-collimated channels were disabled, so the signals in 64 channels were only recorded when the collimated channel observed significant signals. Table 3 lists the radioactive calibration sources used in this paper. Am^{241} decays and emitted photons spontaneously, the others were stimulated and emitted X-ray by Am^{241} radioactivity. We placed the sources along the collimation line about 1 m apart from the scintillator. The distance were adjusted to obtain the trigger rates at $\sim$100 Hz [18,19].

2.2. Result

Figs. 9 and 11 present the energy spectra observed in the collimated channel. When the spontaneous radioactivity of YSO crystal (mainly Yttrium) was observed, the 2 keV scintillation PE yield appeared to be linear. However, since the PE yield was only 1.4 PE, the detection unit could hardly distinguish the spectral detail shown in the reference. When the radioactive sources were applied, the fitted PE yield was linear and was in consistent with which given by the YSO self-scintillation, 0.72 PE/keV. But in addition to the scintillation peaks, a source-induced pedestal was observed covering below 18 keV, and the peaks were all elevated by 7.9 keV (5.7 PE).

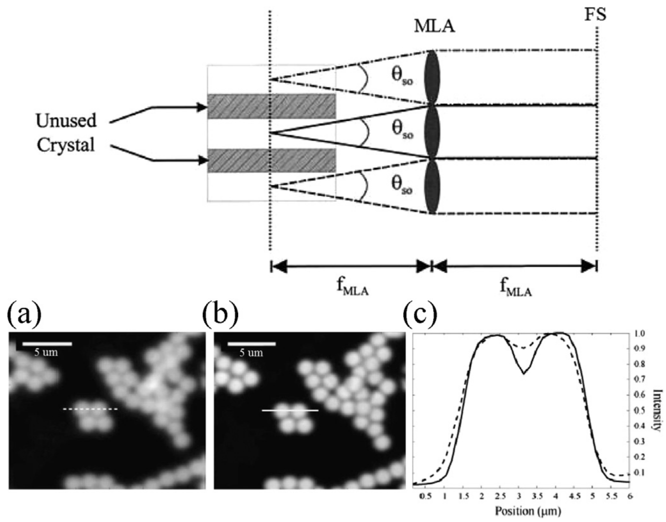

Fig. 6. The upper figure shows an example of the usage of the MLA. With the proper geometrical design, MLA turns the multiple-point-like diffusive emission into parallel light. It is also noted in the figure that a significant portion of the scintillation crystal can be saved. The lower three images present the result of applying MLA. The image taken are 2 μm beads. (a) w/o MLA, (b) w/ MLA, (c) the intensity distributions of the barred locations in (a) and (b), with the corresponding dashed/solid lines used in both cases.

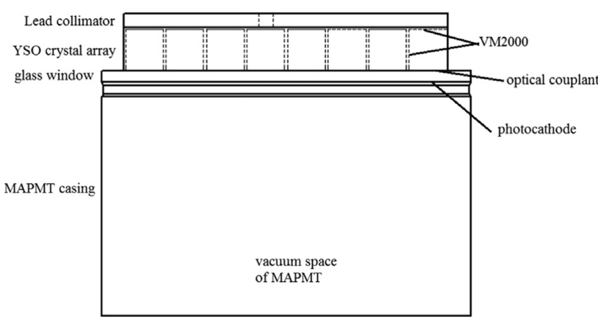

Fig. 7. The side view of the apparatus. The collimator was made of Lead with a ϕ1.0 mm round hole centering Ch. 27.

Table 3
The radioactive calibration sources used in this study.

X-ray source	K_α (KeV)	K_β (KeV)
Am^{241}	59.5[a]	
Tb	44.23	50.65
Ba	32.06	36.55
Ag	22.10	24.99

[a] Note that there is only one energy listed for Am^{241} because we utilized its spontaneous nuclear γ-decay emission, while others were used with their simulated X-ray emissions.

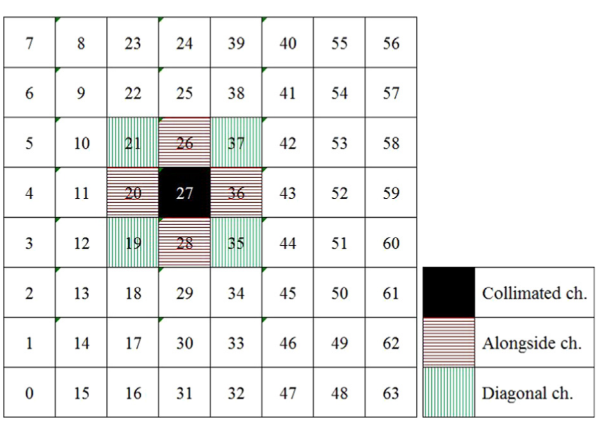

Fig. 8. The naming rule of the channels. The collimated channel was Ch. 27.

In parallel with the calibration of the energy scale, by comparing the signals observed in different channels under the collimated trigger scheme, the signal crosstalk was also quantified. We defined the crosstalk ratio (*CR*):

$$CR = \frac{\text{Pulse height in the channel of discussion}}{\text{Pulse height in the collimated trigger channel}} \quad (1)$$

Averagely 38.27 ± 3.25, 11.22 ± 0.99 and 3.13 ± 0.26 PEs were observed in the collimated, alongside and diagonal channels,

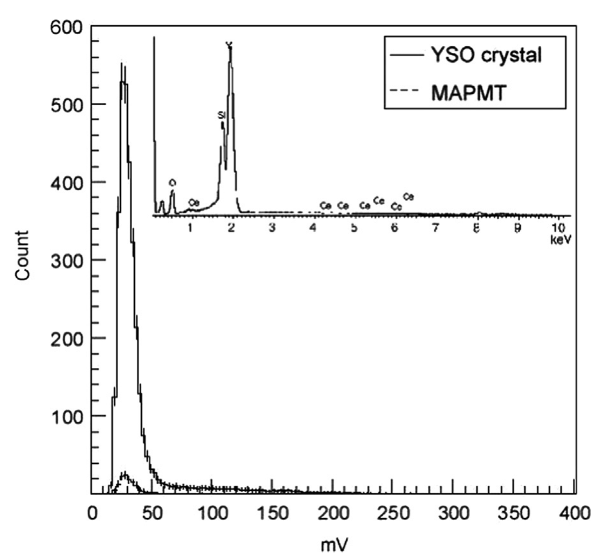

Fig. 9. The spectra of the self-scintillation of the YSO crystal array (solid) and the MAPMT background (dashed), with a reference taken from [18].

respectively (Fig. 12). So the CRs were

$$CR_{alongside} = \frac{11.22 \pm 0.99}{38.27 \pm 3.25} = 0.29 \pm 0.04 \quad (2)$$

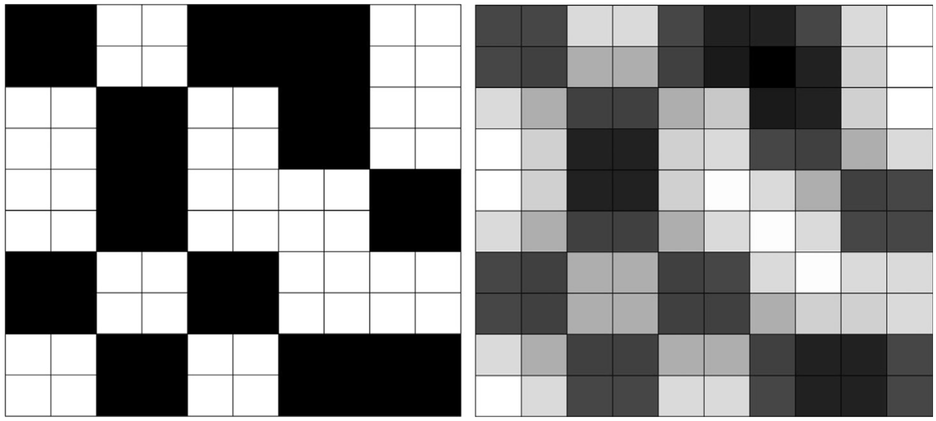

Fig. 10. The comparison of the expected coded mask image (left) and the simulated observation (right). The CRs considered in the alongside and the diagonal channels were 0.29 and 0.08, respectively. The simulation presented the result in 10×10 FS channels, which corresponds to 5×5 coded mask pixels. Both figures are normalized by the highest energy observation and equally scaled in the gray scale.

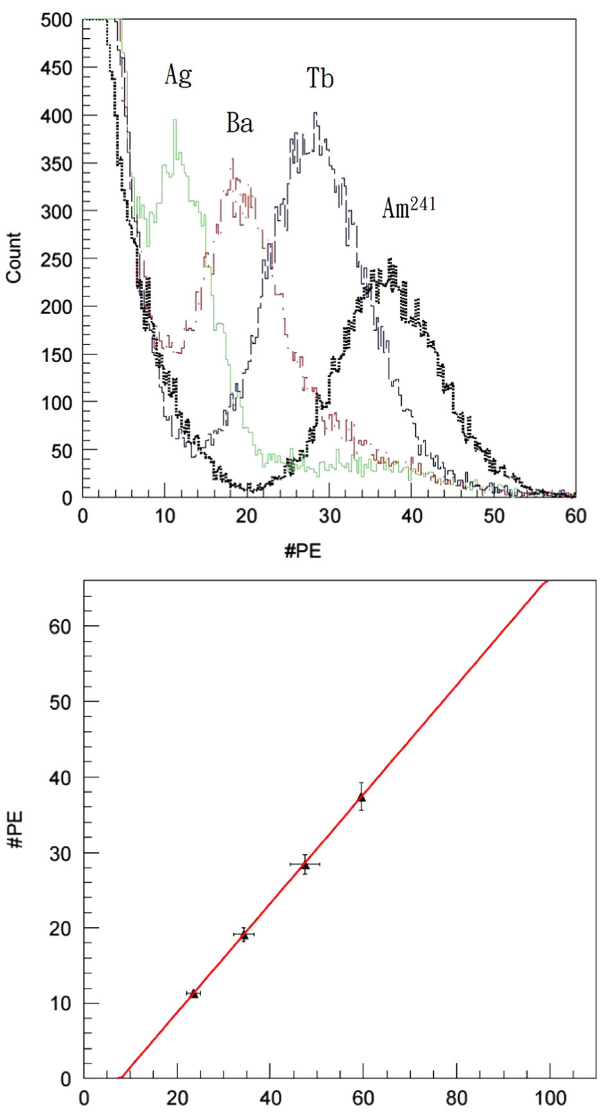

Fig. 11. Top: the energy histograms of Am^{241}, Tb, Ba, Ag, from right to left. Bottom: the linear fit of the PE yields to corresponding energies. The fitting has the slope 0.72 PE/keV and crosses the *X*-axis at 7.9 keV.

$$CR_{diagonal} = \frac{3.13 \pm 0.26}{38.27 \pm 3.25} = 0.08 \pm 0.01 \quad (3)$$

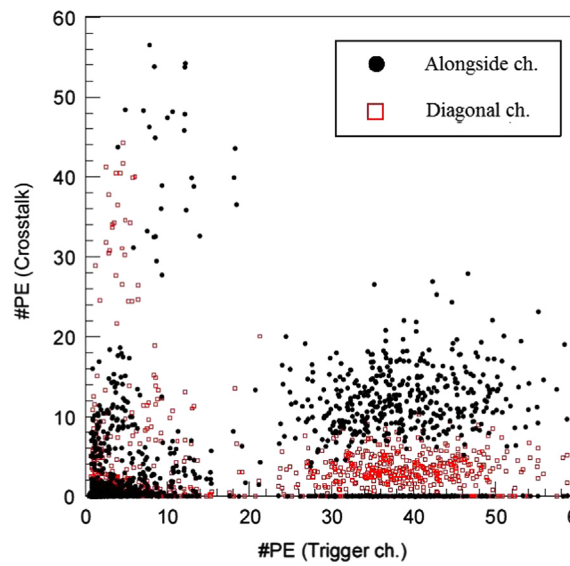

Fig. 12. The 2D histograms of the signals observed in the alongside and the diagonal channels to their trigger signals in the collimated channel. The alongside- and the diagonal-channeled signals are represented by black solid dots and red hollowed squares, respectively. (For interpretation of the references to color in this figure caption, the reader is referred to the web version of this article.)

It was obvious that a significant fraction of the scintillation budget was shared by the non-illuminated channels. If the crosstalk in the remoter channels was omitted, one could conclude that the leakage of the scintillation was about 60%, e.g.

$$\frac{crosstalk}{crosstalk + trigger} = \frac{(0.08 + 0.29) \times 4\ ch.}{1.0 + (0.08 + 0.29) \times 4\ ch.} = 0.60 \pm 0.09 \quad (4)$$

The result indicated that crosstalk led to not only a serious drawback of the detection efficiency, but even crucial, a smearing of the coded mask image. Fig. 10 shows a comparison of the simulated coded mask image considering the crosstalk to the perfectly distinguished one. It was immediately understood it would be unrealistic for *UBAT* to discriminate the X-ray-illuminated and non-illuminated channels of a factor-15 dynamic range, e.g. 10–150 keV, under a simple rate trigger scheme.

3. Simulation

To further resolve the crosstalk issue and search for the possible solutions, we have constructed the simulation package

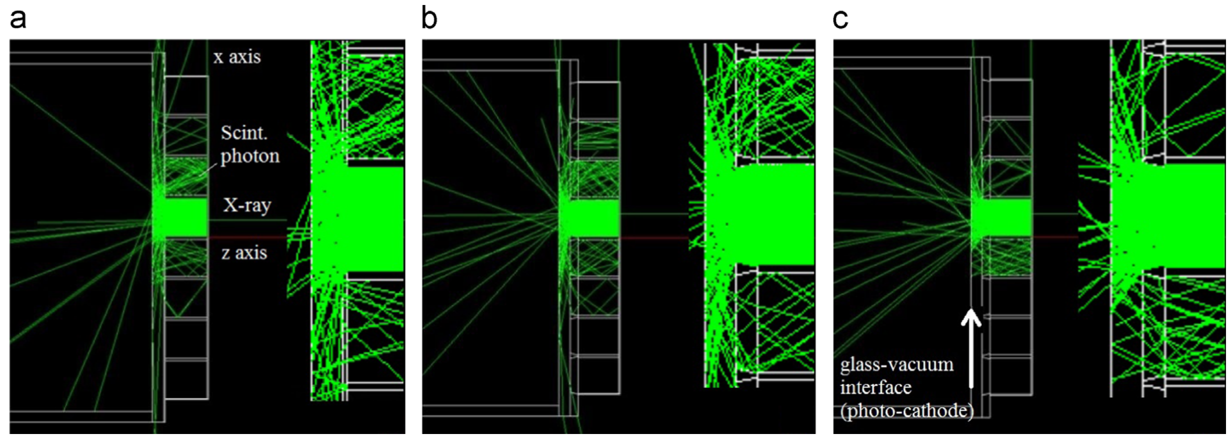

Fig. 13. The side view snapshots of the simulations. Three cases are presented here: (a) no light guide (LG), the original design of the detection unit, (b) with a traditional focusing LG, (c) with an Inverted-Conical LG. The green lines represent the photon paths. It can be seen in the figures the total reflections occurred frequently at the glass–vacuum boundaries, where the photocathodes were. The reflected photons mostly became the crosstalk. By comparing the three cases, it was understood the Inverted-Conical LG suppressed the most crosstalk while the focusing LG worsened the crosstalk issue. (For interpretation of the references to color in this figure caption, the reader is referred to the web version of this article.)

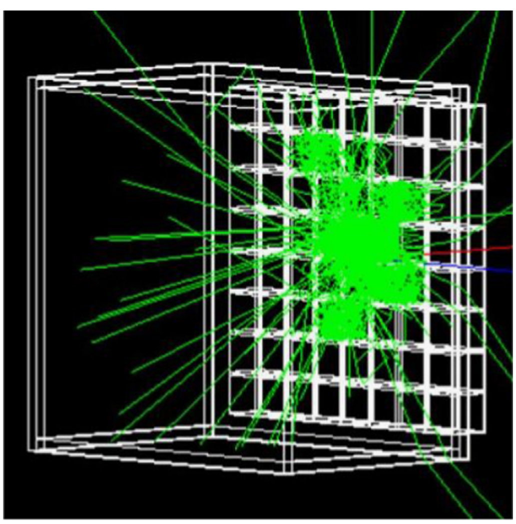

Fig. 14. The simulation screen shot of one X-ray photon event. The green lines represent the paths of the scintillation photons. The primary X-ray photon was collimated and deposited its energy in the collimated YSO crystal cube. (For interpretation of the references to color in this figure caption, the reader is referred to the web version of this article.)

of the *UBAT* FS with GEANT4 [20]. All the components noted in Fig. 7 were constructed in the simulation. Fig. 14 is an example of the screen shot of the simulation. We were able to reproduce the crosstalk in the simulation and interpreted the back-scattering occurred at the photocathode as the key source contributed to at least 70% of the crosstalk. Because the inner space of MAPMT behind the glass window was a vacuum, when the photons traveled from the glass window to the inner space, i.e. penetrating the photocathode, total reflection frequently occurred. And the photons being totally reflected were likely to be observed in the nearby channels as the crosstalk (Fig. 13).

In order to model the response of the photocathode accurately, we had to consider a better model independent from any of the optical surfaces prepared in the GEANT4 library. It was proven in published studies that the photocathode could be modeled nicely by a thin metallic film. The thickness of the film was comparable with the incident wavelength, and its EM wave response was governed by classical electrodynamics. The real and imaginary parts of the refractive index of the photocathode material could be subsequently fitted from the experimental data [21–23]. We explicitly constructed the metallic film model in GEANT4 to simulate the photocathode. Only when the metallic film model was implemented could we simulate the trigger PE yield and the amount of the crosstalk accurately, and stabilized CR within 1%. On the contrary, if the *dielectric_metal* model prepared by GEANT4 was used, the simulation revealed a trivially small amount of crosstalk.

4. Inverted-conical light guide

4.1. Concept

Considering the 29% CR reported in the previous section, if a simple rate trigger scheme is utilized and the 15 keV lower bound of energy is to be maintained, *UBAT* will only be able to discriminate the coded mask pattern of events up to 15/0.29 ∼ 52 keV, which is only 1/3 of the designed energy upper bound. Also learned from the calibration, the expectable signal yield, so as the resolution, are halved by the crosstalk. To cope with the crosstalk issue, we propose the concept of Inverted-Conical LG (IC-LG).

The IC-LG utilizes the orientation inverse to the traditional LG, i.e. with its wide eyelet of the conical channel facing the scintillator.[3] From the simulation, we learned that the crosstalk was mainly caused by the total reflections occurred at the photocathode. To suppress the total reflection, IC-LG is designed to contract the large-angle incidents to be small-angle. It can be seen from Fig. 15, through the internal reflection on the inverted conical channel, IC-LG is capable to redirect all the scintillations to have smaller incident angles. So not just the crosstalk is reduced, we also expect a good fraction of the crosstalk photons are recovered to be the signal.

A simulation comparison of the situations without LG, with an IC-LG and with a NIC-LG is shown in Fig. 13. It is clear the emission from IC-LG exhibits smaller open angle and the illumination area on the photocathode plane. The reflections travel into the neighboring crystals are also less. Another advantage shown in Fig. 15 is that IC-LG can be made much thinner than the scintillation array or the

[3] The traditional orientation is addressed as non-inverted conical (NIC) in the following content.

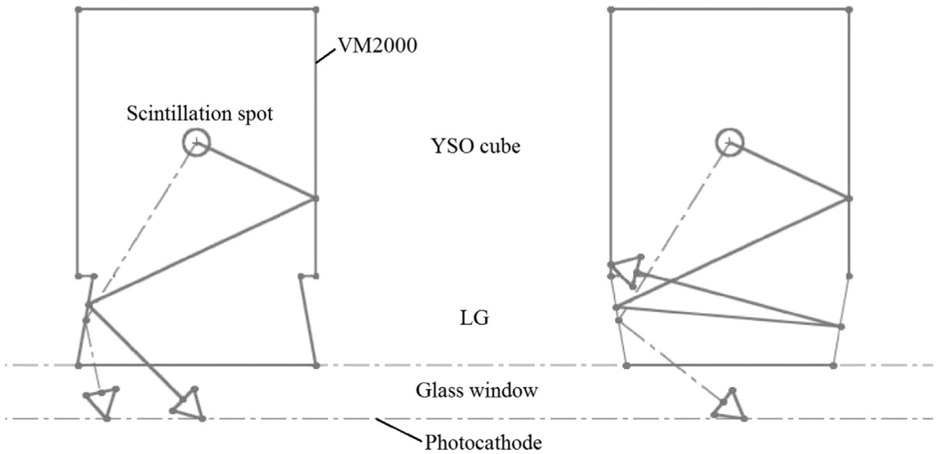

Fig. 15. The illustration of the concept of "inverted-conical" LG. The setup presented here includes two YSO cubes connect to one IC-LG channel (left) and one NIC-LG channel (right). The dashed and solid lines represent the small and large angle incidents, respectively. It can be seen from the figure, through reflection, IC redirects the photons to have smaller angles. On the contrary, although the NIC may look like focusing the scintillation, when the LG has a comparable size of the glass window, the functionality of focusing is negligible, but it certainly enlarges the incident angles of all the scintillations.

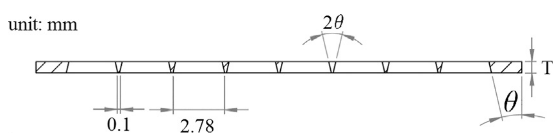

Fig. 16. The cross section view of IC-LG. The parameters to be optimized are the thickness (T) and the conical angle (θ). The upper side in this figure is the scintillator side, the lower side is MAPMT.

traditional LG but still effective. This characteristic implies the narrow eyelet is only slightly smaller than the wide side, so the shielding and the signal reduction are minimized. Also it is important to the general design of *UBAT* (so as in other applications), since the geometry is prefixed, any non-trivial alteration to the FS could significantly affect the performance of the coded mask aperture camera.

4.2. Optimization

We constructed the IC-LG in the simulation of *UBAT* and inserted it between the scintillator array and MAPMT. The IC-LG was optimized in two parameters, the thickness (T) and the conical angle (θ) (Fig. 16). The IC channels were consecutively arranged in an 8×8 matrix identical to the scintillator array. The 100 μm grid gapping between the wide eyelets was left for practical engineering. So the width of the wide eyelet was 2.88 (pixel size $-\frac{0.1}{2}\times2$ (both side) $=2.78$ mm, and the width of the narrow eyelet was derived from $2.78-2T\tan\theta$.

Different combinations of T and θ were simulated in the range 0.6–1.5 mm and $-5°$-$20°$, negative angle represents the NIC configuration. In additional to CR and the signal yield, Crosstalk Index (CI) was also used as an indicator to the optimization:

$$CI \equiv \frac{\Sigma(\text{ch. separation} \times \text{local signalyield})}{(\Sigma\text{ch. separation}) \times \text{collimated ch. signal yield}} \quad (5)$$

Eq. (5) summed over all the channels in the same row and the column of the collimated channel, e.g. ch. 27 was the collimated channel, the equation summed up ch. 4, 11, 20, 36, 43, 52 and ch. 24, 25, 26, 28, 30, 31. The corresponding channel separations were 1 for ch. 20, 26, 28, 36; 2 for ch. 11, 25, 29, 43; 3 for ch. 4, 24, 30, 52; 4 for ch. 59. CI was regarded as the weighted indicator to the overall condition of the crosstalk among the FS.

Fig. 17 presents the optimization of the crosstalk to θ. When $\theta<0°$, CR was enlarged compared to which when $\theta>0°$. The result coincided with the expectation IC-LG could reduce the crosstalk while NIC-LG might enlarge it. CR and CI posed similar trends and minimums appeared at $\theta=13.50°$ and $\theta=15.67°$, respectively. The result could be interpreted as the steeper angle suppressed more crosstalk, when the crosstalk in the further channels was taken into consideration, a larger angle was favored. Nevertheless, the $\sim2°$ difference was actually trivial for the minimal regions were about $4°$ across.

Fig. 18 presents the optimization of the signal yield. The IC-LG enhanced the signal yield by at most 25% when $T<12$ mm. The signal yield decreased by $\sim$3% for every 0.1 mm increase in T. It was also demonstrated in the simulation NIC-LG suppressed the signal yield and the suppression was severer with steeper NIC angle. The optimal angle of 108.9% signal yield appeared at $9.67°$. The result indicated IC-LG had the capability of focusing the photons and enhancing the signal yield identical to MLA.

Because the primary motivation of the LG study was the crosstalk reduction, $(\theta,T)=(13°,0.6\text{ mm})$ was regarded as the optical solution, for it gave the least CR while also enhanced the signal yield. According to the simulation, the optimized IC-LG would enhance the signal yield by 7.2% and reduce CR to 15.8%, i.e. 45% CR reduction from the calibrated CR of the detection unit.

5. Sample test

5.1. Fabrication

Fig. 19 presents the photos and the schematics of the sample IC-LG. The sample was made of 6061 Aluminum alloy through CNC machining with <1 μm position tolerance then polished through chemical anodic brightening. The fabrication was cost -friendly yet the end product had geometric accuracy ~0.5 μm and the surface roughness <100 nm. The perimetral frame was designed to support the delicate grid-like LG. The end product was as mechanically endurable as the scintillator array and the MAPMT.

5.2. Result

The signal comparison of LG-free, IC-LG and NIC-LG cases is presented in Fig. 20. Before applying the LG, CR was 0.293 ± 0.024. The sample IC-LG reduced 38.86 ± 3.22% crosstalk but acquired 6.376 ± 0.053% PE yield reduction. The resulting CR with IC-LG was

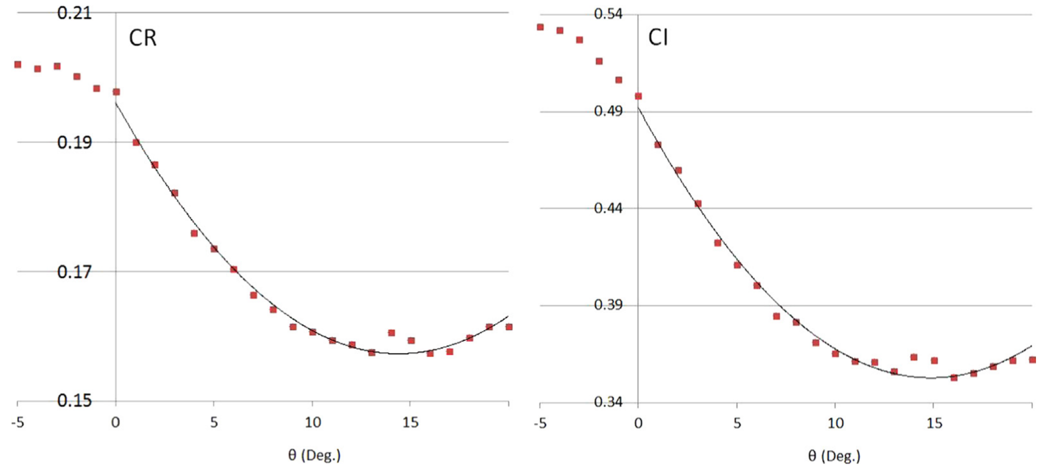

Fig. 17. The simulated crosstalk versus the conical angle θ at T = 0.8 mm. The right- and left-handed panels are the CR and CI, respectively. The overlaid fittings are the 2nd-order polynomials. The minimal points of the fitters are at 13.50° and 16.57° for CR and CI, respectively. The NIC-LG is also shown in the figures as the negative angles.

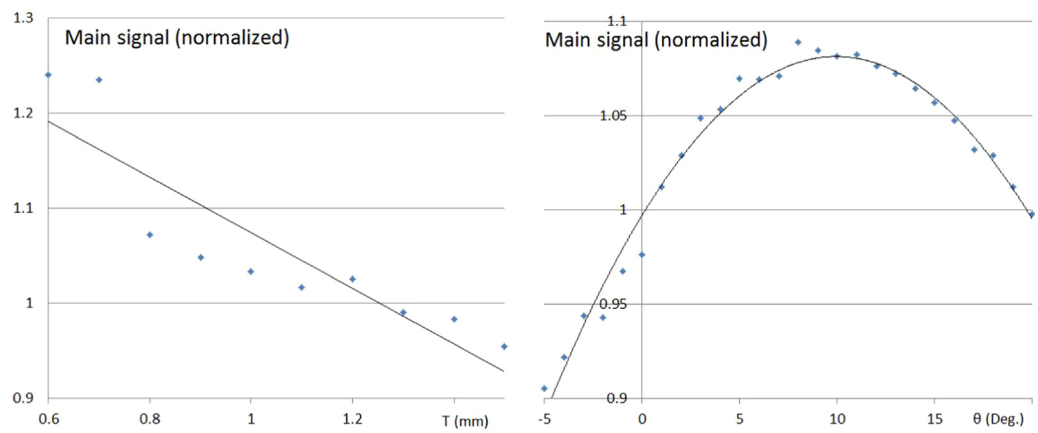

Fig. 18. The simulated signal yield versus the thickness T (left panel) and conical angle θ (right panel), $\theta = 13°$ and T0.8 mm were assumed in the figures, respectively. The overlaid fittings are the 1st- and 2nd-order polynomials. The maximal point of the signal-to-θ fitter is at 9.67° which gives 8.9% signal enhancement. The NIC-LG is also shown in the figures as the negative angles. The signal yield was normalized by which before applying a LG.

0.195 ± 0.016. As a comparison, the sample was also inserted under the NIC orientation, i.e. 180° flipped. The NIC orientation gave CR 0.244 ± 0.020 and $11.47 \pm 0.95\%$ PE yield cutback. To understand Fig. 20, the LG-free detection unit observed the largest signal, IC-LG second, and NIC-LG the last in both the collimated and the alongside channels. However, IC-LG exhibited the collimated signal peak close to the LG-free condition but the alongside signal peak close to the NIC-LG condition. The net consequence was an amelioration of reducing CR from 0.29 to 0.20.

Before the amelioration, the alongside and the diagonal CRs were 29% and 8%. With the aid of IC-LG, CRs became 20% and $< 2\%$ in the alongside and diagonal channels, respectively. The simulated coded mask images are shown in Fig. 22. We also repeated the energy calibration with IC-LG, all the procedure was identical to Section 2. The result is shown in Fig. 21. With IC-LG, *UBAT* FS detection unit had linear signal yield 0.69 PE/keV.

6. Conclusion

UFFO is designed to be the first GRB observatory capable of responding to the UV–visible signals of GRBs within 1 min; *UBAT* is the primary prompt emission trigger telescope in *UFFO-p* responsible for delivering the event directions. To achieve the rapid direction determination, *UBAT* is designed to operate under the coded mask aperture camera scheme. So it is crucial that the focal surface detection units must confidentially discriminate the coded mask pattern.

In this paper, we demonstrated the energy and the image crosstalk calibrations of the *UBAT* focal surface detection unit. The signal yield was 0.72 PE/keV. A serious crosstalk issue of $\sim 29\%$ relative signal height was identified in the pixels closing the X-ray illuminated one. A simulation of the detection unit was then constructed to resolve the issue. Through the simulation study, we pointed out more the 70% of the crosstalk was caused by the total reflections occurred at the photocathode. After identifying the source of the crosstalk, we proposed the Inverted-Conical light guide which utilized the inverted orientation of the traditional focusing LG as a possible solution. The Inverted-Conical light guide was optimized in the simulation and fabricated. The end product reduced the crosstalk and the signal yield by 39% and 6%, which resulted in the reduction of CR from 29% to 20%.

The metallic Inverted-Conical light guide was made much thinner than the components of the detection unit. Unlike many other light guides, it preserves the original geometry of the scintillation detector. As shown in the simulation, the Inverted-

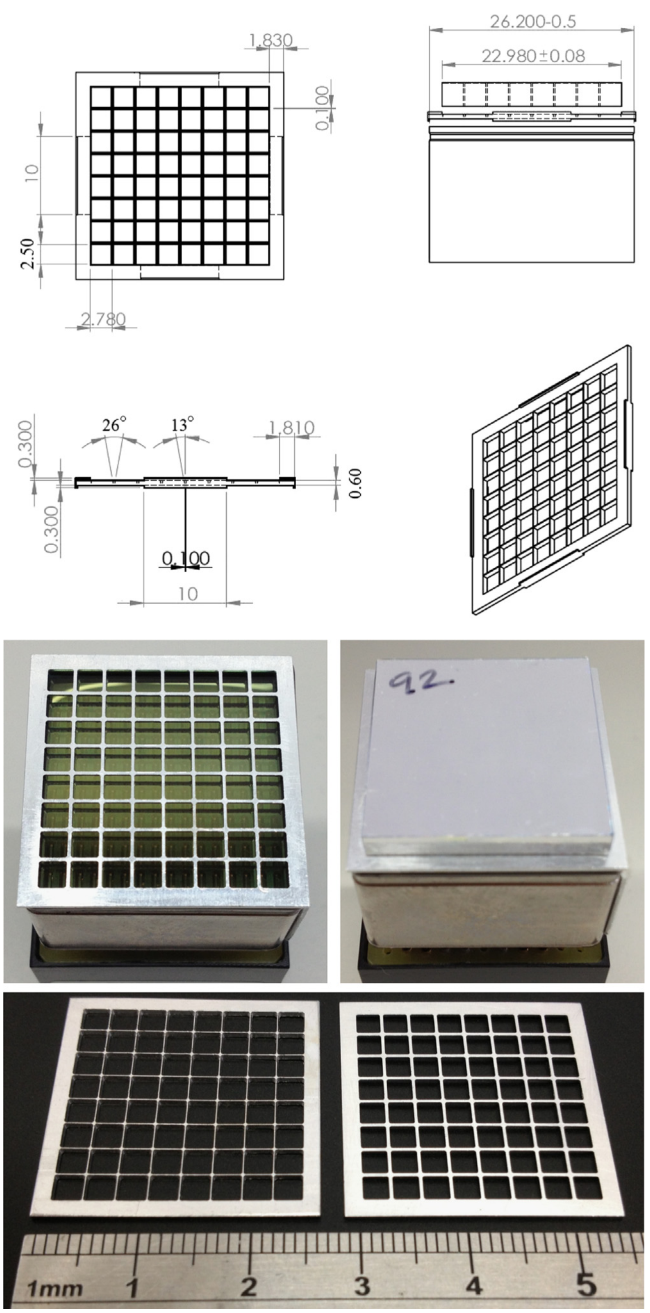

Fig. 19. The schematics and the photos of the sample IC-LG and its assembly with the scintillator array and MAPMT.

Conical light guide also has the advantage over other light guides that it reduces the crosstalk and enhances the signal yield at the same time. Since the sample light guide utilized consecutive structure of the conical channels, one might think of the MLA as a similar comparison (Fig. 6) [26–28]. Indeed MLA has been demonstrated to have the ability of focusing the light and enhancing the image quality, and it has been widely applied to delicate optical products. However, MLA is obviously too fragile for space missions like *UFFO*, and it is much more expensive and less customizable. IC-LG preserves the advantages of MLA but also largely improves its disadvantage of fragileness.

UFFO-pathfinder is scheduled to launch in 2015. Since the flight model of *UFFO-p* was completed and has been integrated to the

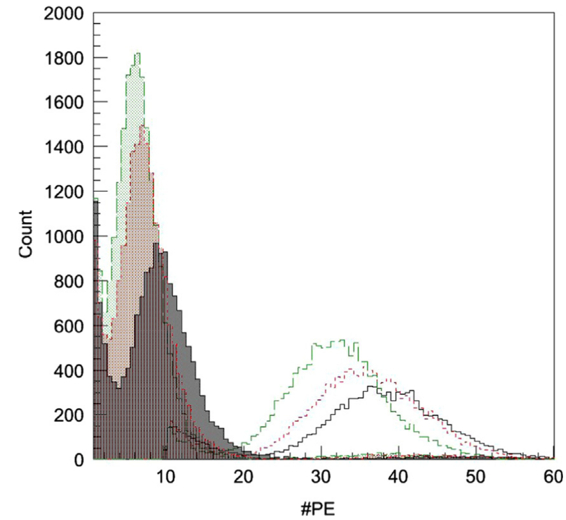

Fig. 20. The signal histograms of the cases LG-free (solid lined), IC-LG (short-dashed lined) and NIC-LG (long-dashed lined). The signals observed in the collimated and alongside channels are represented by the hollowed and shaded areas, respectively. The calibration source was Am^{241}. The signal smaller than 10 PE in the collimated channel was excluded in this figure for better clearance.

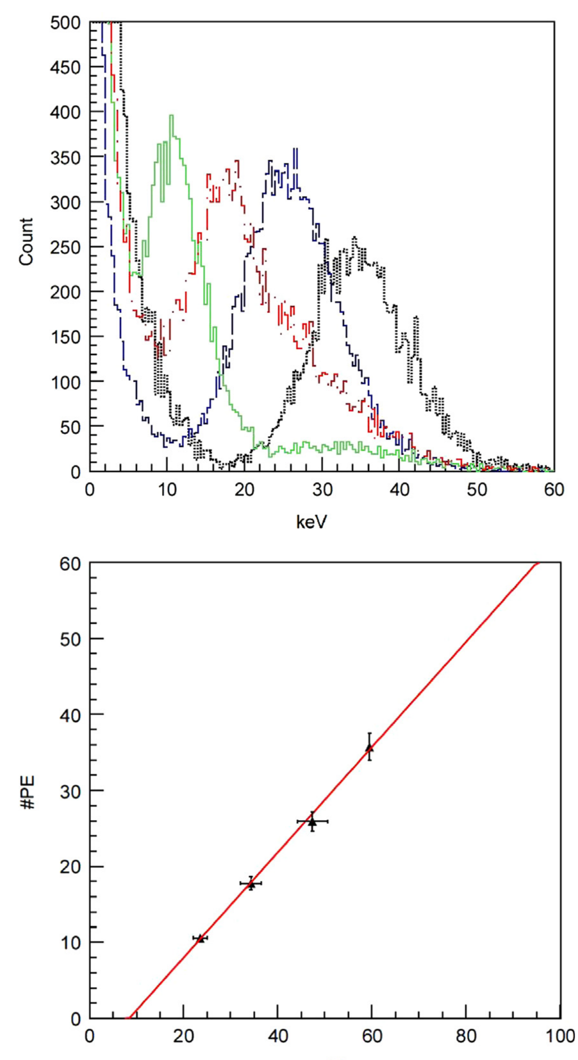

Fig. 21. Left: The IC-LG-ameliorated signal histograms of, peaks from right to left, Am^{241}, Tb, Ba and Ag. Right: The peak #PEs versus the corresponding X-ray energies. The linear fit shows the slope 0.69 PE/keV. The error bars were taken as K_α–K_β.

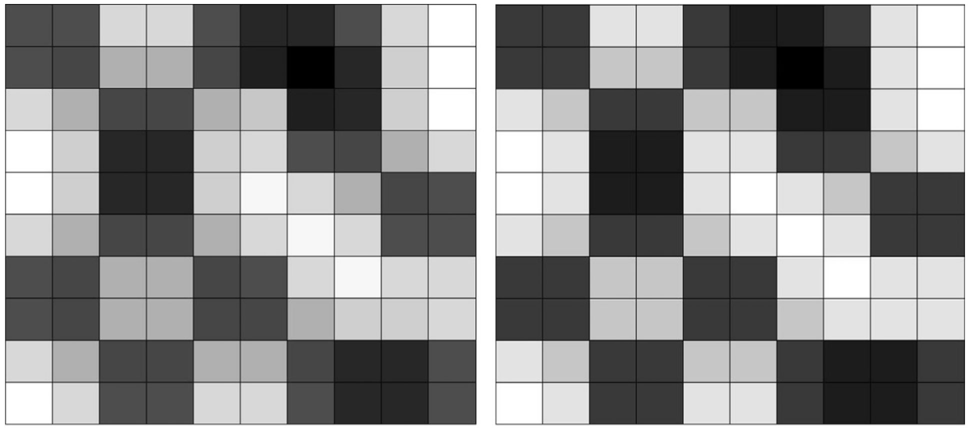

Fig. 22. The comparison of the simulated scintillation detections of the coded mask image before (left) and after (right) the amelioration with IC-LG. Both figures are normalized by the channels of the highest energy and equally scaled in the gray-scale.

platform of *Lomonosov*, Inverted-conical light guide was not implemented in *UBAT*. However, we are still looking forward to the future utilization of Inverted-Conical light guide to future *UFFO*-100.

Acknowledgments

This work was supported by Taiwan's Ministry of Science and Technology (MOST) Vanguard Program (102-2628-M-002-010), Taiwan's National Space Organization (NSPO) supported by MOST, the Creative Research Initiatives program (RCMST) of MSIP/NRF in Korea, the Spanish MINECO through project number AYA 2009-14000-C03-01/ESP, AYA 2012-39727-C03-01/ESP and AYA 2011-29936-C05-01, the program of development of Lomonosov Moscow State University, and NRF SRC program 2010-0027910 of Center for Galaxy Evolution Research.

References

[1] P. Roaming, et al., Space Science Reviews 120 (2005) 95.
[2] I.H. Park, New Journal of Physics 15 (2013) 023031.
[3] A. Panaitescu, et al., Monthly Notices of the Royal Astronomical Society 287 (2008) 497.
[4] K.L. Page, et al., 2009. arXiv:astro-ph/0907.4578.
[5] P. Jakobsson, et al., Astrophysical Journal 617 (2004) L21.
[6] N. Gehrels, et al., Astrophysical Journal 689 (2008) 1161.
[7] W.-K. Zheng, et al., Research in Astronomy and Astrophysics 9 (10) (2009) 1103.
[8] S. Jeong, et al., Optics Express 21 (2) (2013) 2263.
[9] J. Lee, Gamma-ray Burst: 15 Years of GRB afterglow, EPS Publ. Seri., vol. 61, 2013, p. 525.
[10] S.D. Barthelmy, et al., Space Science Reviews 120 (2005) 143.
[11] M. Turler, Image gallery, iSDC webside (http://www.isdc.unige.ch/), Univ. Geneva, 2005.
[12] H.E. Ruthfuss, et al., IEEE-Nuclear Science Symposium N24 (2007) 196.
[13] J. Beringer, et al., Particle Data Group, Physical Review D D86 (2012) 010001.
[14] P. Yeh, et al., Modern Physics Letters A 19 (2004) 1117.
[15] Y.S. Velikzhanin, et al., Nuclear Instruments and Methods in Physics Research Section A 552-3 (2006) 477.
[16] K.-X. Huang, Master Thesis, Phys. Dept., N. T. U., unpublished, 2007.
[17] C.-P. Chang, Master Thesis, Phys. Dept., N. T. U., unpublished, 2011.
[18] E. Zycha, et al., Journal of Alloys and Compounds 451 (1–2) (2008) 286.
[19] M.I.T. Dept. of Phys. 2007, in: X-Ray Physics, from Amersham Data Sheet 11196.
[20] S. Agostinelli, et al., Nuclear Instruments and Methods in Physics Research Section A 506 (2003) 250.
[21] M. Born, et al., Principle of Optics, Pergamon Press, Oxford, 1964.
[22] D.T. Motta, et al., Nuclear Instruments and Methods in Physics Research Section A 539 (2005) 217.
[23] M.E. Moorhead, et al., Nuclear Instruments and Methods in Physics Research Section A 378 (1996) 162.
[24] H. Spieler, Introduction to Radiation Detector and Electronics, LBNL, 1999.
[25] H. Harano, et al., IEEE Transactions on Nuclear Science 52-6 (2005) 3147.
[26] C.D. Brewer, et al., Applied Optics 41-21 (2002) 4411.
[27] M.-K. Wei, et al., Optics Express 12–23 (2004) 5777.
[28] A. Orth, et al., Optics Express 20 (2012) 13522.